Available online at www.sciencedirect.com
ScienceDirect
Trans. Nonferrous Met. Soc. China 35(2025) 1490−1505
Transactions of Nonferrous Metals Society of China
www.tnmsc.cn

Effects of annealing temperature on mechanical properties and corrosion behaviors of biodegradable Mg−3Zn−0.2Ca−2Ag alloy wires

Qing-hui WANG[1], Shan-shan LIANG[2], Fu-song YUAN[2],
Bo PAN[3], Peng-fei SUN[3], Jin-hui WANG[1], Bo-yu LIU[1], Hong-xiang LI[1]

1. State Key Laboratory for Advanced Metals and Materials,
University of Science and Technology Beijing, Beijing 100083, China;
2. Center of Digital Dentistry, School and Hospital of Stomatology, Peking University, Beijing 100081, China;
3. Plastic Surgery Hospital, Chinese Academy of Medical Sciences and Peking Union Medical College,
Beijing 100144, China

Received 16 October 2023; accepted 28 April 2024

Abstract: In response to the interest in degradable magnesium staples for oral and maxillofacial surgical procedures, high-performance Mg−3Zn−0.2Ca−2Ag alloy wires were reported. The impact of annealing temperature on the mechanical properties and corrosion behavior of the alloy wires was investigated. Results indicated that an increased annealing temperature led to grain growth, reduced the volume fraction of the second phase, and lowered dislocation density, causing decreased strength. The alloy annealed at 150 °C exhibited the highest elongation (19.6%) due to uniform and fine grains, along with lower dislocation density. Microscopic observation, and electrochemical and immersion tests highlighted the significant influence of annealing temperature on corrosion rates. Alloy wires annealed at 150 °C demonstrated superior corrosion resistance, which is attributed to small and uniform grains, low stress, and a well-distributed nano-second phase. Finally, the alloy wires annealed at 150 °C exhibited enhanced comprehensive properties, making them good candidates for degradable staples.

Key words: biodegradable Mg alloy; magnesium staples; mechanical properties; micro-galvanic corrosion; biocompatibility

1 Introduction

With the development of medical devices, more and more anastomotic devices are being used in clinical surgeries [1]. In recent years, biodegradable materials such as iron (Fe), zinc (Zn), magnesium (Mg) and their alloys have received significant attention as medical implants due to their outstanding degradable properties [2]. Mg and its alloys, known for their rapid degradation, present distinctive advantages, as seen in studies validating pure Mg (HP-Mg) as a stapler [3]. Various Mg alloys, such as Mg−2.5Nd−0.21Zn−0.44Zr (JDBM) [4] and Mg−2.2Nd−0.1Zn−0.4Zr (JDBM-2) [5], exhibit excellent biocompatibility and stability. ZHANG et al [6] developed a biodegradable staple made by micro-arc oxidation (MAO) and polylactic acid (PLLA)-coated AZ31 magnesium alloy wire for colon anastomosis. The degradation time of the staples corresponds to the healing time of the colon wound. This suggests that we can adjust the degradation time of magnesium alloy through process regulation to meet various requirements.

In order to obtain high-performance of Mg alloy

Corresponding author: Hong-xiang LI, Tel: +86-10-62332928, E-mail: hxli@skl.ustb.edu.cn
https://doi.org/10.1016/S1003-6326(25)66762-8

wires, various methods have been adopted to regulate their microstructure. MA [7] systematically studied the influence and mechanism of alloying elements (Sn, Mn, Zr, Ge, and Ag) in extruded Mg−1.0/2.0Zn−0.2Ca alloys. For example, MA et al [8] changed the quantity and distribution of the $Ag_{17}Mg_{54}$ phase by regulating the content of Ag elements, thereby altering the properties of the alloy. They also found that by adding a small amount of Ag element (2 wt.%) into Mg−3Zn−0.2Ca alloy, the alloy wires with a diameter of 0.5 mm achieved tensile strength, yield strength, and elongation of 326.1 MPa, 314.5 MPa, and 19.6%, respectively. The yield strength exceeded other similar materials reported domestically and internationally [9]. Additionally, it is common to add rare earth elements and aluminum (Al) to enhance the properties of the alloy. However, Al causes some neurological diseases [10], and rare earth elements induce liver poisoning [11]. Drawing deformation is an essential process for preparing magnesium alloy wires. ZHANG et al [12] obtained uniformly dispersed nanoparticles (with an average diameter of about 14.3 nm) with a high yield strength of about 285 MPa and good ductility of about 11.8% through cold drawing. This indicates that the microstructure and corresponding mechanical properties of Mg−Zn−Ca alloys can be regulated through large plastic deformation. LU et al [13] demonstrated that heat treatment could alter the volume fraction and grain size of the second phase in the Mg−3Zn−0.3Ca alloy, thereby significantly affecting its corrosion rate. In summary, there are two main methods for regulating the performance of degradable magnesium staples: alloy design and process improvement.

Despite the progress of degradable Mg wires, current degradable Mg alloy wires do not meet the gradual degradation requirement after being placed in the human body for about two weeks. In addition, degradable magnesium alloys should also have high strength and toughness. Therefore, in response to the particular environment of the oral and throat region, it is necessary to develop a biodegradable magnesium alloy staple with high strength and toughness that can be degraded in the body within about two weeks without adding harmful elements. The Mg−3Zn−0.2Ca−2Ag alloy wire recently developed by our research group has been confirmed to be a promising candidate material for preparing staples for oral and throat surgery. However, the impact of annealing temperature on the microstructure, mechanical properties, and corrosion behavior of this alloy wire remains unexplored. For this aim, the strengthening and corrosion mechanisms of the alloy wire are discussed in this work. This study provides an excellent material choice for the degradable staples applied in oral and maxillofacial surgery.

2 Experimental

Alloys of nominal composition Mg−3Zn−0.2Ca−2Ag (wt.%.) were smelted using high-purity Mg (99.99 wt.%), high-purity Zn (99.999 wt.%), high-purity Ag (99.999 wt.%), and Mg−Ca (20 wt.%) master alloys in an electric resistance furnace at 750 °C under a CO_2/SF_6 protective atmosphere. The melt was cast into a mild steel mold to obtain an alloy ingot with a diameter of 40 mm and a height of 90 mm. Then, the alloy ingots were homogenized at 350 °C for 24 h, and the ingots were processed into a cylinder with a diameter of 35 mm and a height of 15 mm for subsequent extrusion. The extrusion was carried out with a ratio of 19:1 at 330 °C. Finally, an alloy wire with a diameter of 0.5 mm was obtained by combining drawing with annealing from an initial diameter of 8 mm. The process was carried out at room temperature using a drawing machine and a diamond die. The drawing speed was set at 30 mm/s, with a single-pass deformation ranging from 5% to 10%. Intermediate annealing was conducted at 200−300 °C for 30 min. It was lubricated with machine oil to minimize friction during drawing. Further, the effect of different annealing temperatures on the microstructure and properties of alloy wires was studied. In this study, annealing was conducted at temperatures of 120, 150, and 240 °C for 30 min. The alloy wires subjected to annealing at different temperatures in this study all originated from the same ingot. The chemical composition of the as-cast alloy was analyzed using X-ray fluorescence spectrometry (XRF). The results indicated concentrations of 3.24 Zn, 0.13 Ca, and 1.78 Ag, balanced with Mg.

The samples for microstructure characterization parallel to the extrusion direction (ED) were ground

through SiC paper and polished with diamond grinding paste. The microstructures of the specimens were observed using scanning electron microscopy (SEM, Phenom XL) equipped with energy-dispersive X-ray spectroscopy (EDS, Phenom XL). SEM images were captured in backscattered electron (BSE) mode at an accelerating voltage of 20 kV. Electron backscatter diffraction (EBSD, Oxford Cswift) characterized the local microstructure and texture. Transmission electron microscopy (TEM, Talosf200x) provided a detailed visual description of the types, morphologies, and distributions of the precipitated phases. The samples for the TEM test were prepared by artificial polishing to a thickness of 30−40 μm and ion thinning technology. The tensile tests were performed with an extensometer (50 mm in gauge length) in the CMT6104 testing machine, and the initial rate was 1×10^{-3} mm/s.

The corrosion behaviors of the alloy wires were investigated by immersion tests and electrochemical tools in the simulated body fluid (SBF) solution. The ratio of the surface area to solution volume was 1 cm^2: 40 mL according to ASTM G31-72, and the corrosion morphologies were analyzed by SEM. The composition of SBF solution was 6.800 g/L NaCl, 0.200 g/L$CaCl_2$, 0.400 g/L KCl, 0.100 g/L $MgSO_4$, 2.200 g/L $NaHCO_3$, 0.126 g/L Na_2HPO_4, and 0.026 g/L NaH_2PO_4 [14,15]. Finally, a cleaning solution (200 g/L CrO_3 and 0.1 mol/L $AgNO_3$) was used to remove the degradation products. The degradation morphologies of the sample before and after the removal of corrosion products were observed using SEM and EDS. The degradation rate (R) was calculated according to ASTM-G31-72 using the formula $R=(KW)/(ADT)$ [16−18], where K is a constant ($K=8.76\times10^4$), W means the mass loss, A means the area, T means the exposure time, and D means the density. Three duplicate samples were measured to ensure the reproducibility of the results.

The CS310H electrochemical testing system was used to obtain dynamic polarization and electrochemical impedance spectroscopy (EIS) at 37 °C in the SBF solution. EIS was conducted at frequencies ranging from 0.1 Hz to 100 kHz with a perturbing signal of 5 mV. EIS analysis was also conducted at an open circuit potential, with an interference signal of 5 mV. Electrokinetic polarization was done at a scanning rate of 1 mV/s. Scanning Kelvin probe force microscopy (SKPFM) was used to determine the corrosion tendency of different material microstructures based on the measurement of the voltage potential difference on the surface of the local scale sample.

3 Results

3.1 Microstructure

Figure 1 displays the microstructures of annealed Mg−3Zn−0.2Ca−2Ag samples characterized by SEM. The image reveals a substantial amount of white spherical second phases with varying sizes precipitated throughout the Mg matrix. However, the number and distribution of precipitates differed at various annealing temperatures. The EDS analysis (Table 1) shows that the precipitates were mainly composed of the phases containing Mg, Zn, and Ag elements, as well as the phases containing Mg and Zn elements. Statistical analysis revealed that the contents of the second phase were 6.02 vol.% in as-drawn samples, and 9.02, 8.65, and 6.64 vol.% in samples annealed at 120, 150, and 240 °C, respectively. The volume fraction of the secondary phases increased with the annealing treatment, and higher annealing temperature resulted in lower volume fractions. Further characterization is needed due to the relatively low resolution of SEM in analyzing microstructure changes.

Figure 2 shows the microstructure evolution of the Mg−3Zn−0.2Ca−2Ag alloy wires after heat treatment at different temperatures. Two secondary phases were distributed in all samples: the dark large-sized phase mainly at grain boundaries, and the small-sized phase uniformly distributed within grains. The selected area electron diffraction (SAED) patterns confirmed that these phases were $Ag_{17}Mg_{54}$ and Mg_2Zn_{11}, respectively (inset in Figs. 2(a, b)). In addition, dislocation cells formed by dislocation entanglement were observed in samples annealed at 120 and 150 °C, with uneven grain boundaries and parallel dislocation distributions within the grains. However, from Figs. 2(c, d), dislocation entanglements were less frequent and only appeared in very few positions in samples annealed at 150 °C. Despite this, many precipitates hindered dislocation migration. In

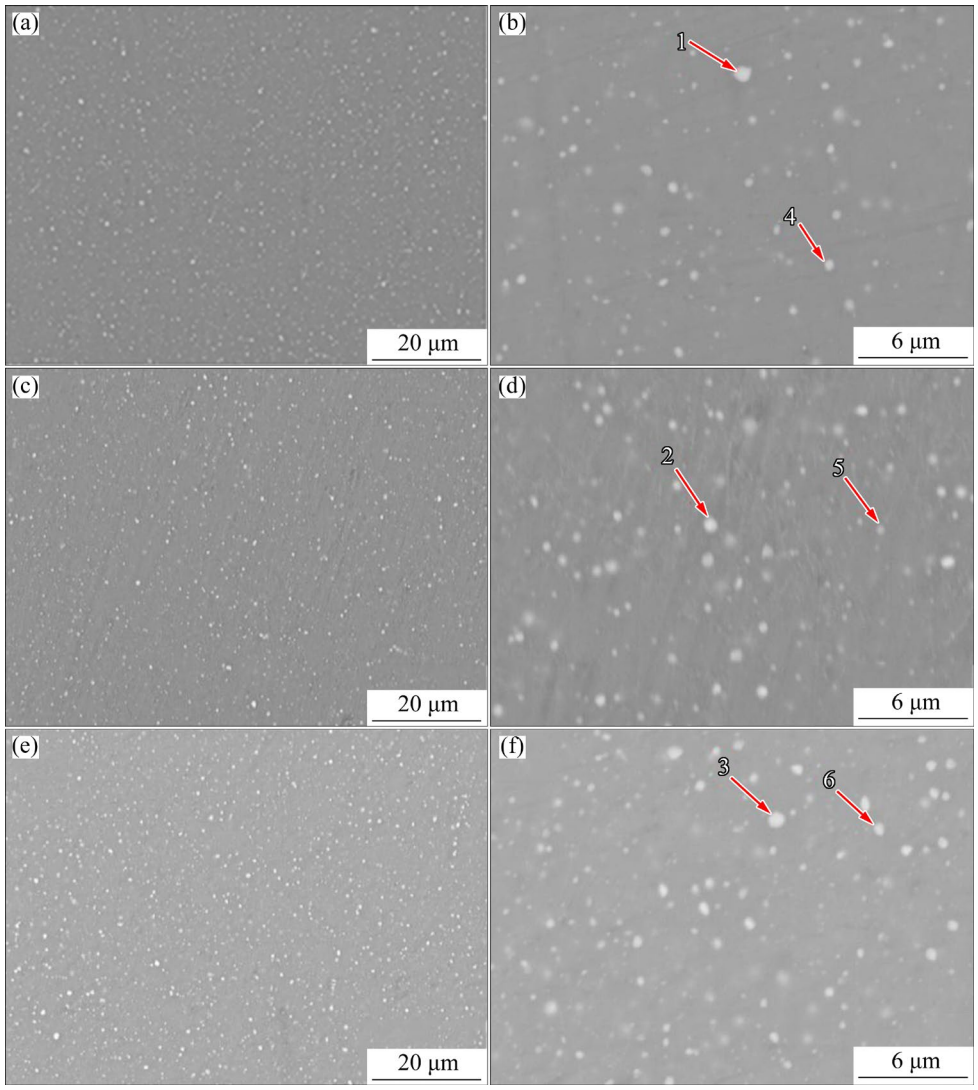

Fig. 1 SEM images of Mg−3Zn−0.2Ca−2Ag alloy wires annealed at different temperatures: (a, b) 120 °C; (c, d) 150 °C; (e, f) 240 °C

Table 1 EDS analysis of precipitated phases (at.%)

Point in Fig. 1	Mg	Zn	Ag
1	93.55	4.12	2.33
2	94.35	3.53	2.12
3	94.16	3.76	1.64
4	97.06	2.94	–
5	98.19	1.81	–
6	97.51	2.48	–

Fig. 2(e), small nanoscale Mg_2Zn_{11} precipitates were evenly distributed at 240 °C, albeit in fewer quantities compared to 150 °C. The larger $Ag_{17}Mg_{54}$ phases were predominantly localized at the grain boundaries. We observed no dislocation cells or walls, with only a small number of dislocations distributed along these boundaries.

To analyze the texture, orientation maps, pole figures (PFs), and inverse pole figures (IPFs) are presented in Fig. 3 with the projection plane parallel to the drawing direction. In Fig. 3(a), the mean size for samples annealed at 120 °C was 4.0 μm. With increasing temperature, grain size initially decreased to 3.0 μm at 150 °C, and then gradually grew to 5.7 μm at 240 °C. Elongated un-DRXed regions were observed in samples annealed at 120 °C, surrounded by small grains. As the annealing temperature rose, the recrystallization level increased. The grains at 150 °C gradually transformed into equiaxed grains. When the annealing temperature increased to 240 °C, the recrystallization was basically completed, and the grains grew significantly.

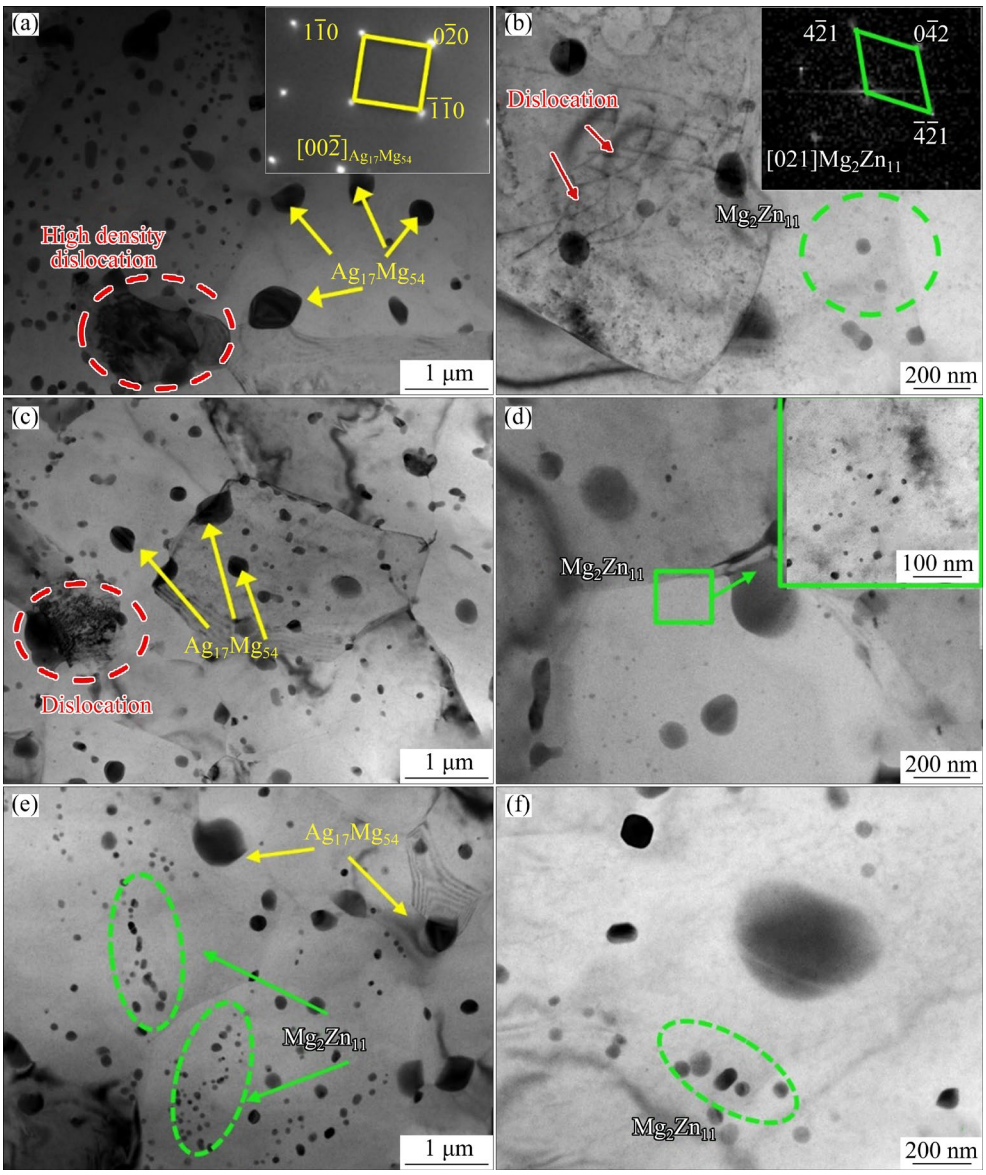

Fig. 2 Bright-field TEM images and corresponding SAED patterns of Mg−3Zn−0.2Ca−2Ag alloy wires annealed at different temperatures: (a, b) 120 °C; (c, d) 150 °C; (e, f) 240 °C

Due to the limited slip systems of Mg alloy, plastic deformation at room temperature is challenging. Large deformation or annealing can cause changes in grain orientation. Figure 3 illustrates the effect of annealing temperature on texture evolution. In Fig. 3(a), the basal plane of samples annealed at 120 °C was symmetrically distributed in the transverse direction (TD) direction, exhibiting a traditional $(0001)\langle 01\bar{1}0\rangle$ deformation texture. When the annealing temperature increased to 150 °C, the (0001) plane gradually aligned parallel to the ED direction. IPFs (Fig. 3(b)) confirmed a mixed morphology with different components, including $\langle 01\bar{1}0\rangle$ and $\langle \bar{1}2\bar{1}0\rangle$ parallel to ED, and the direction between $\langle 01\bar{1}0\rangle$ and $\langle \bar{1}2\bar{1}0\rangle$ parallel to ED. As the temperature increased to 240 °C, the (0001) surface progressively shifted toward the ED direction, and the axial direction fully turned toward $\langle \bar{1}2\bar{1}0\rangle$, presenting a texture of $(0001)\langle \bar{1}2\bar{1}0\rangle$ //ED. In addition to the distribution difference, the peak intensity of textures increased from 7.75 (120 °C) to 7.99 (150 °C) and then to 8.23 (240 °C).

Geometrically necessary dislocations (GND) is considered a residual dislocation accumulated to adapt to local lattice strain. The considerable residual dislocation considered as GNDs to accommodate local strains was retained due to the un-DRX deformation. Figure 4 illustrates the concentrated high-density GND regions within large deformed

grains and grain boundaries. The distribution of calculated GNDs in the alloy samples is shown in Fig. 4, with an average value of $\rho_{GND}=9.0\times10^{14}$ m^{-2} at 120 °C, $\rho_{GND}=3.3\times10^{14}$ m^{-2} at 150 °C, and $\rho_{GND}=1.4\times10^{14}$ m^{-2} at 240 °C. This indicates that higher temperatures reduced the density of residual dislocations and alleviated local lattice strain.

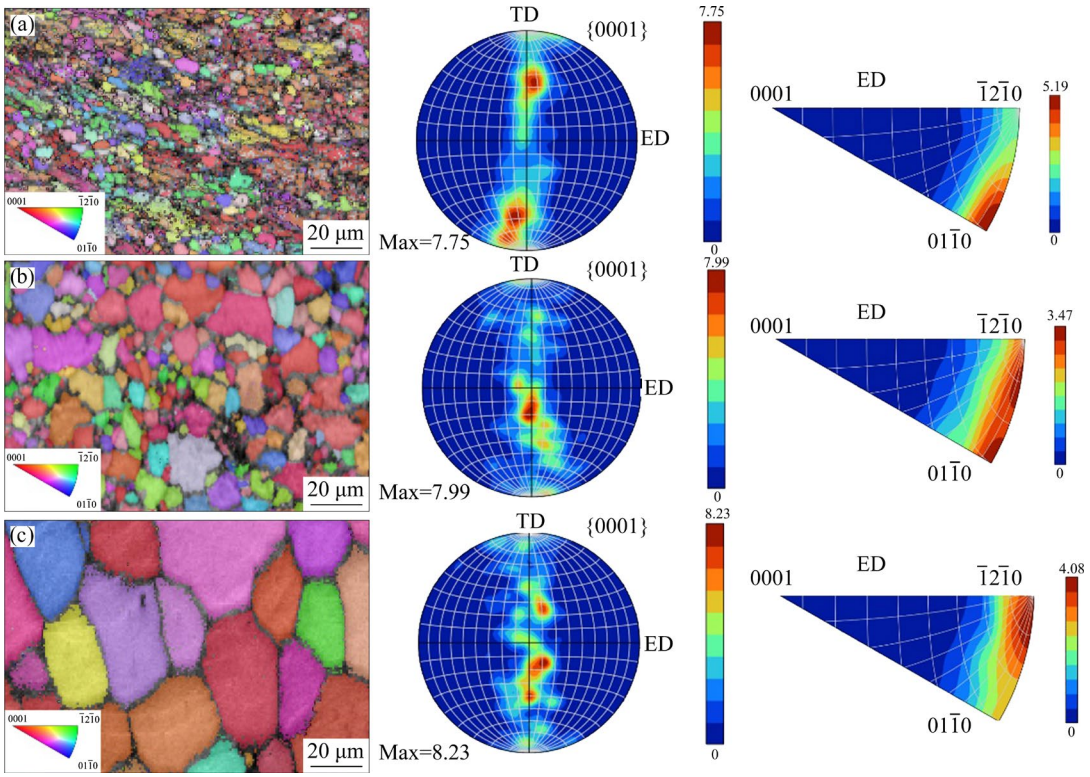

Fig. 3 EBSD orientation maps and corresponding (0001) PFs and IPFs showing textures of Mg−3Zn−0.2Ca−2Ag alloy wires annealed at different temperatures: (a) 120 °C; (b) 150 °C; (c) 240 °C

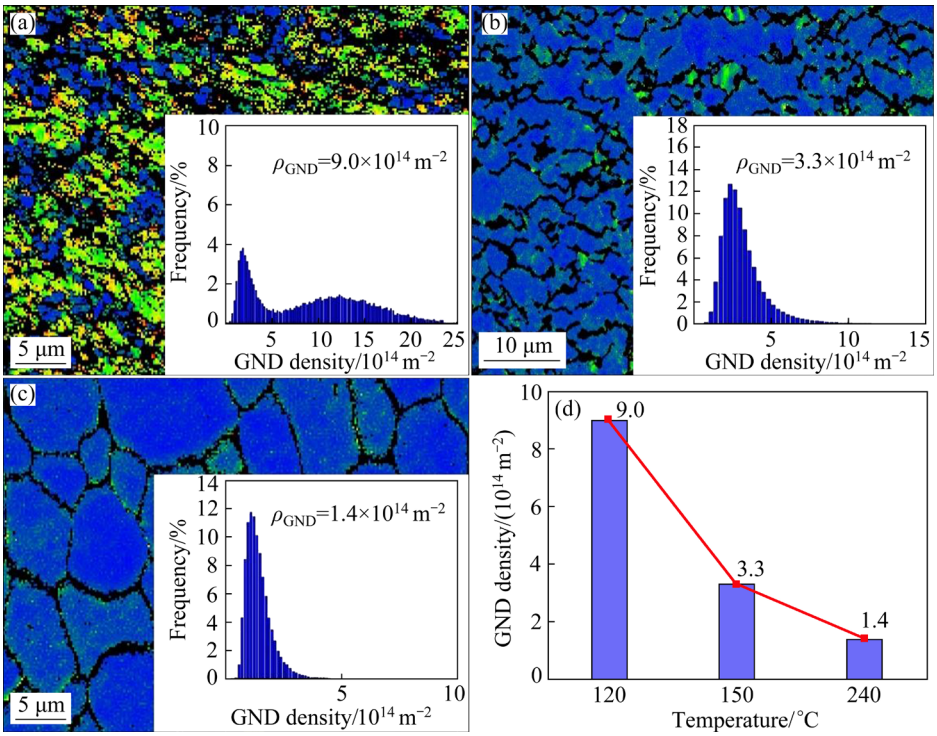

Fig. 4 GND density graphs for samples annealed at temperatures of 120 °C (a), 150 °C (b) and 240 °C (c), and density comparison at different temperatures (d)

3.2 Mechanical properties

Figure 5 shows the mechanical properties of Mg−3Zn−0.2Ca−2Ag alloy wires annealed at 120, 150, and 240 °C, with detailed information in Table 2. In this study, the tensile yield strength (TYS) of Mg−3Zn−0.2Ca−2Ag alloy wire decreased from 354.38 to 314.52 MPa as the annealing temperature increased from 120 to 150 °C, reaching 242.42 MPa at 240 °C. However, elongation initially increased and then decreased with the rise in annealing temperature. Compared with the samples annealed at 120 °C, the elongation of the samples annealed at 150 and 240 °C alloys increased by 276.2% and 127.7%, respectively. Figures 5(b−d) show the fractographs of the studied alloys after tensile tests. The fracture surfaces exhibited a combination of cleavage facets and dimpled regions. Several cracks between cleavage facets suggest that the presence of un-DRXed regions may degrade ductility by serving as crack nucleation sites. Under the same tensile conditions, samples annealed at 120 °C exhibited the largest cleavage facet area, while those annealed at 150 °C was the smallest. The difference in cleavage facet area depends on the degree of recrystallization in these alloys. The increase in annealing temperature decreased the area of cleavage facets as the DRX fraction increased.

Figure 6 exhibits the comparison of the mechanical and corrosion properties among our alloy wires and other magnesium alloy wires. From Fig. 6(a), it can be seen that the tensile strength of Mg−3Zn−0.2Ca−2Ag (120 °C) alloy wire was very prominent, but its ductility was poorer than other alloys. The Mg−3Zn−0.2Ca−2Ag (150 °C) alloy wire demonstrated the best comprehensive mechanical properties, and no harmful elements such as rare earth and Al were added to the magnesium alloy wires. The stapler material used in oral and maxillofacial surgery requires a fast degradation rate. From Fig. 6(b), it can be seen that the alloy wires in this work could attain the fastest degradation rate, whether in Hank's solution, SBF, DMEM, or in vivo. This shows that alloy wires can meet the requirement of degradable magnesium staples. Therefore, this alloy wire is expected to become a good candidate material for making the anastomosis staplers for oral and maxillofacial surgery.

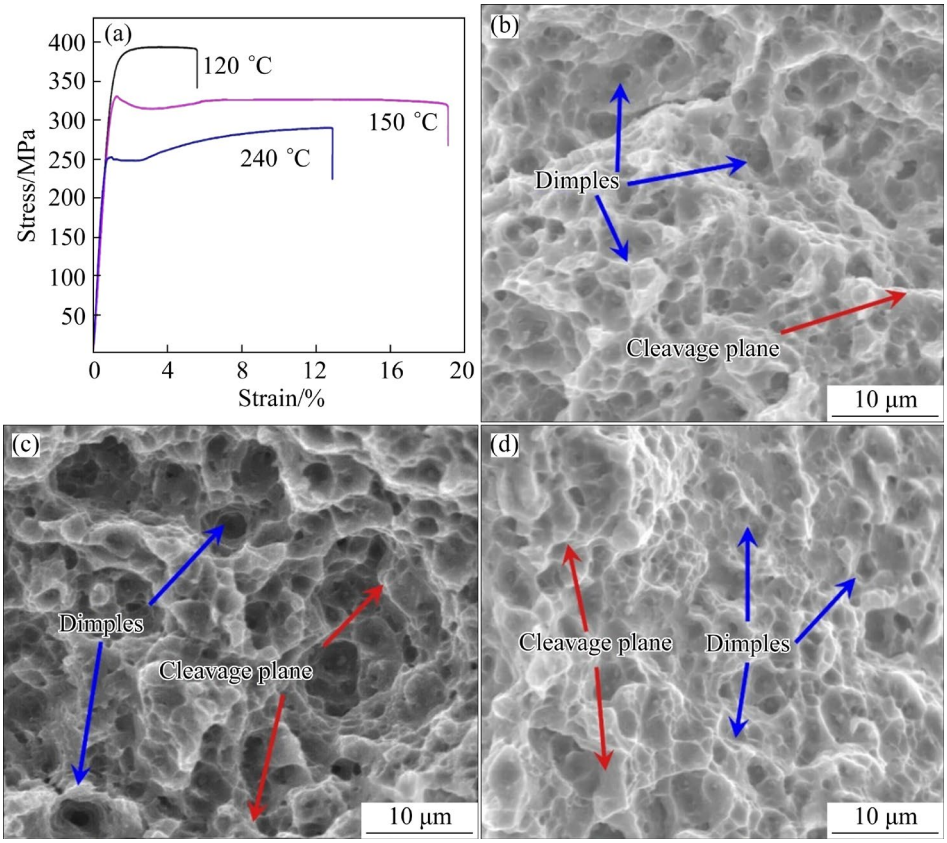

Fig. 5 Tensile curves of samples annealed at 120, 150, and 240 °C (a), and surface morphologies of tensile fracture for alloy wires at 120 °C (b), 150 °C (c) and 240 °C (d)

Table 2 Mechanical properties of Mg−3Zn−0.2Ca−2Ag alloys annealed at different temperatures

Temperature/°C	UTS/MPa	TYS/MPa	EL/%
120	393.90	354.38	5.2
150	326.07	314.52	19.6
240	290.17	242.42	11.8

3.3 Corrosion behaviors

Figure 7 shows a comparison of the mass loss rate of the Mg−3Zn−0.2Ca−2Ag alloys after immersion in the SBF solution for 24 h. It can be seen that the corrosion rate of each alloy was relatively fast, and the corrosion rate of the sample annealed at 150 °C was slightly slow.

Figure 8 depicts the corrosion morphologies of the samples before and after removing corrosion products following 24 h immersion in SBF solution. The corrosion patterns of alloy wires were nearly identical. The wire surface was covered with a loose corrosion product film, along with significant, deep corrosion cracks (Figs. 8(a, c, e)), primarily resulting from water loss and shrinkage during the drying process. EDS analysis shows that the corrosion products on the surface mainly include O, Mg, P, Ca, N, Zn, and Ag elements, indicating the presence of diverse degradation products. Based on our EDS results and relevant literature [16,29,30], these corrosion products likely included MgO, $Mg(OH)_2$, $MgCO_3$, Ag_2O, $Zn(OH)_2$, $CaCO_3$, and $Ca_{10}(PO_4)_6(OH)_2$. Among them, $Mg(OH)_2$ was the primary component of the corrosion film. Notably, Cl^- ions in the SBF solution could easily penetrate the film, reacting with $Mg(OH)_2$ to form soluble $MgCl_2$, thereby compromising the integrity of the corrosion film. Additionally, $Mg(OH)_2$ served as a nucleation site for hydroxyapatite, a major inorganic component of human and animal bones known for its excellent biocompatibility [31]. Upon removal of the corrosion products, the wire exhibited severe corrosion, losing its metallic luster. Deep corrosion pits along the drawing direction were visible, as well as various sizes of pitting and river-like corrosion pits. The formation of pitting corrosion was mainly associated with the second phase precipitated in the matrix.

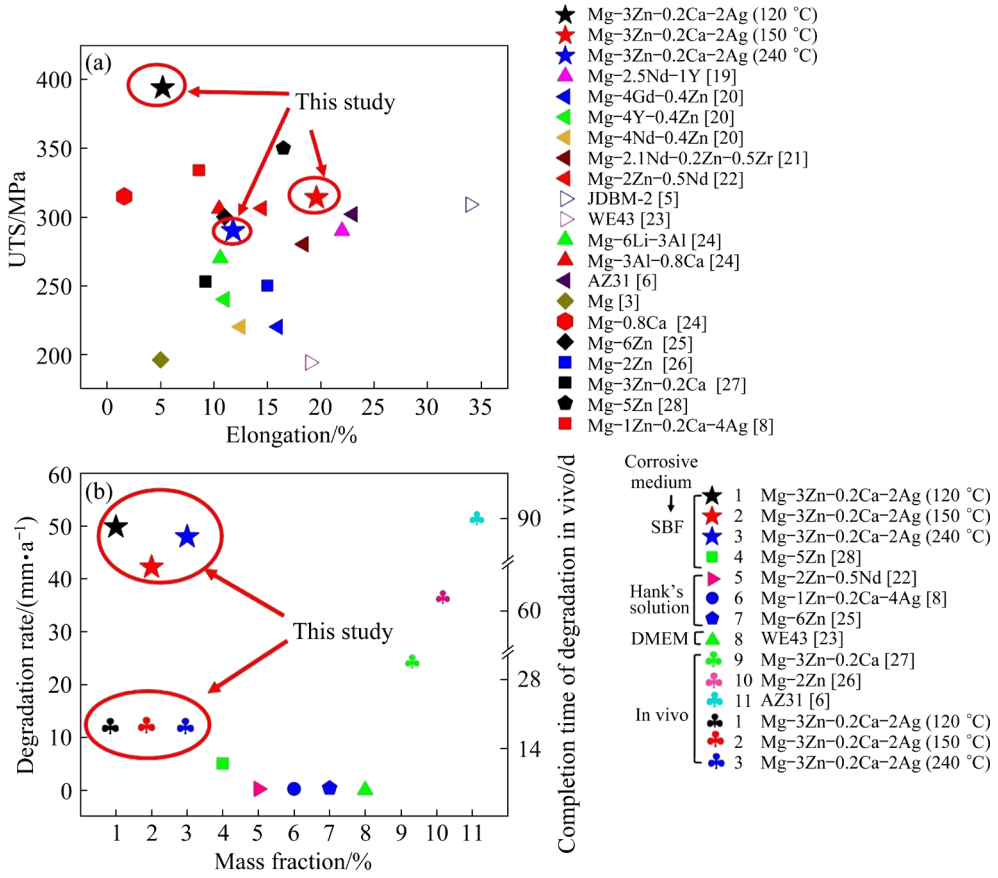

Fig. 6 Comparison of yield strength, fracture elongation, and degradation rate of multi-pass cold-drawn Mg−3Zn−0.2Ca−2Ag alloy annealed at different temperatures and other Mg alloy wires: (a) Ultimate tensile strength (UTS) and elongation; (b) Degradation rate [3,5,6,8,19−28]

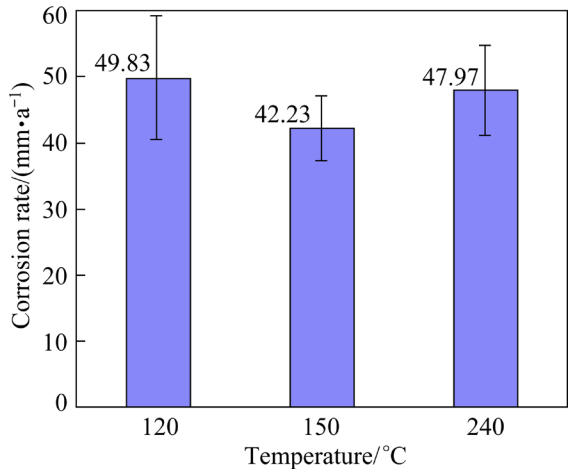

Fig. 7 Corrosion rates of Mg−3Zn−0.2Ca−2Ag alloy wires annealed at different temperatures in SBF solution

The potentiodynamic polarization diagrams at three conditions examined are shown in Fig. 9. The Tafel extrapolation method yielded electrochemical parameters, including corrosion current density (J_{corr}) and corrosion potential (φ_{corr}), listed in Table 3. The corrosion potential generally indicates the difficulty of corrosion occurrence. As shown in Fig. 9, the corrosion potential followed the order of 150 °C>120 °C>240 °C. This suggests that corrosion at 150 °C was slightly less prone than the other two alloys, though the difference was insignificant. The finer and more uniformly distributed second phase in samples annealed at 150 °C contributed to the formation of a more uniform corrosion layer, thereby improving the corrosion resistance. The corrosion current density,

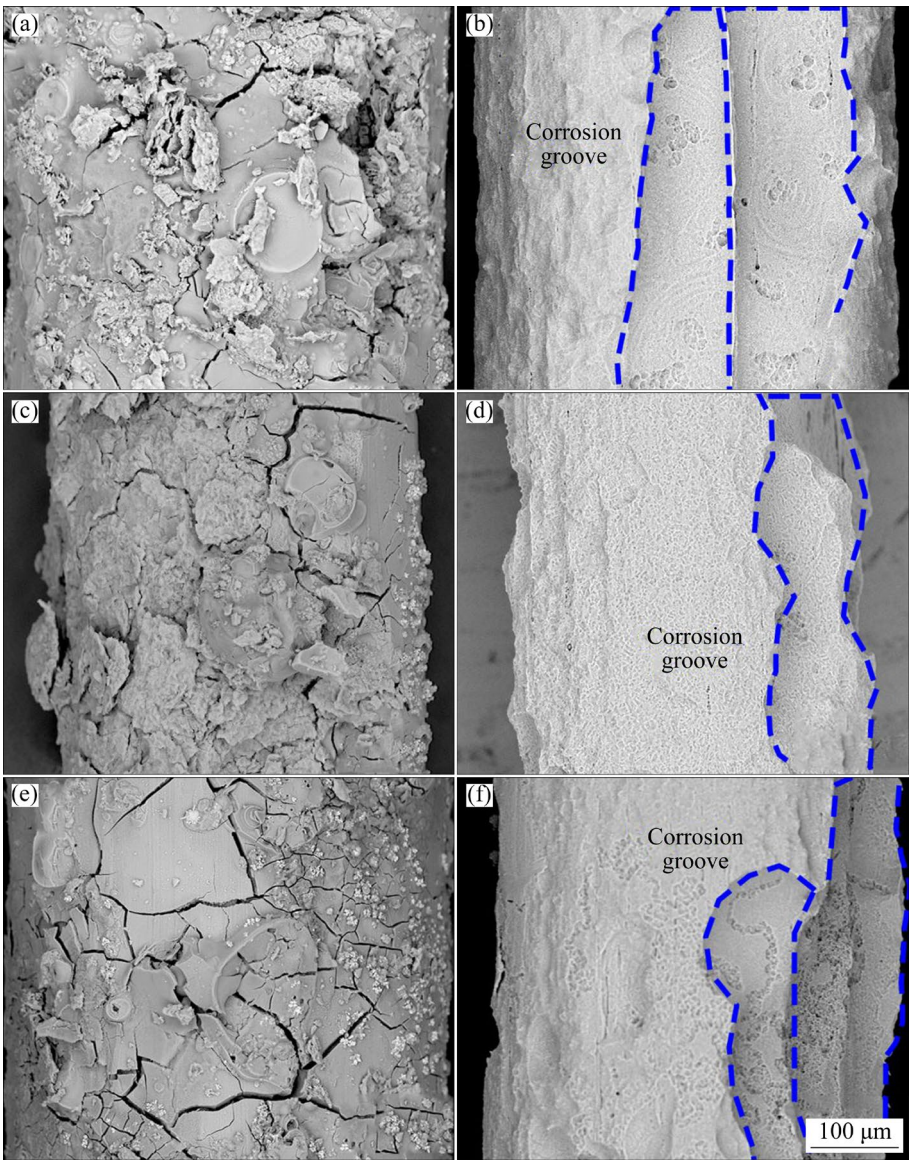

Fig. 8 Surface morphologies of Mg−3Zn−0.2Ca−2Ag alloy wires annealed at different temperatures before and after removing corrosion products: (a, b) 120 °C; (c, d) 150 °C; (e, f) 240 °C

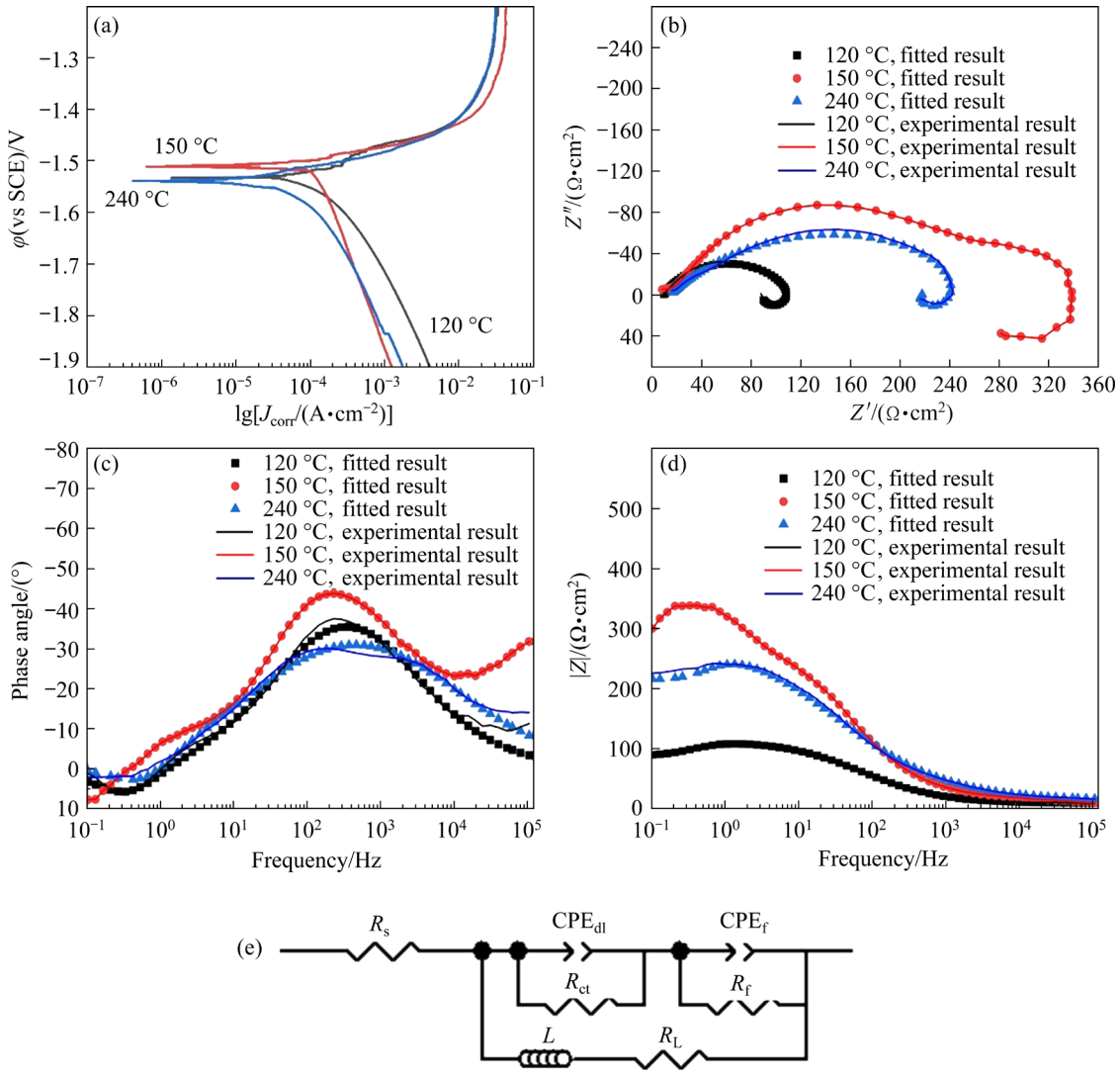

Fig. 9 Polarization curves and EIS results of Mg−3Zn−0.2Ca−2Ag alloy wires annealed at different temperatures in SBF solution: (a) Polarization curve; (b) Nyquist plot; (c, d) Bode plot; (e) Equivalent circuit

Table 3 Polarization curve fitting data of Mg−3Zn−0.2Ca−2Ag alloy wires annealed at different temperatures in SBF solution

Temperature/ °C	φ_{corr}(vs SCE)/ V	J_{corr}/ (μA·cm^{-2})	β_a/ mV	β_c/ mV
120	−1.5093	138.77	49.753	241.74
150	−1.5036	114.46	33.828	378.59
240	−1.5428	118.52	104.14	326.00

to some extent, reflects the corrosion rate. The corrosion current density of samples annealed at 120 °C was slightly higher than those of the other two alloys, in line with the reported mass loss results.

The EIS results are plotted in Figs. 9(b−d) with the Nyquist and Bode (impedance module and phase angle shift) representations. The Nyquist plot shows three semicircles (a high-frequency capacitance ring, a mid-frequency capacitance ring, and an inductance ring) that could be fitted by an equivalent circuit. The high-frequency capacitance loop corresponds to the double-layer formation at the Mg matrix−electrolyte interface, indicating charge transfer resistance. The mid-frequency capacitance loop relates to the presence of the surface film [32]. The low-frequency inductive loop suggests insufficient protective function of the surface film and corrosion nucleation during the initial stages of localized corrosion [33]. A natural oxide film was formed on magnesium alloy surfaces, containing defects, like micro-pores or cracks. If these defects are uniformly distributed, a series combination of two resistors and a capacitor

can be employed [34]. According to the electrochemical equivalent circuit model proposed by LIU et al [34] for fitting electrochemical data, as depicted in Fig. 9(e), the corresponding fitting data are presented in Table 4, where R_s is the electrolyte resistance, i.e., the resistance of the SBF solution; CPE_{dl} and R_{ct} are the interface diffusion double-layer capacitance and charge transfer resistance between material surface and solution, respectively. The higher R_{ct} value for the alloy annealed at 150 °C suggests superior corrosion resistance. CPE_f and R_f are corrosion product film capacitance and resistance, respectively. The low-frequency trough also confirms the existence of inductance. R_L and L represent resistance and inductance, respectively, indicating the onset of localized corrosion [34]. n is the distribution index and the value range is $0<n<1$. The larger the impedance modulus, the better the protective ability of the corrosion product film. Figure 9(d) confirms better corrosion resistance in the samples annealed at 150 °C. However, further tests are needed to comprehensively study corrosivity, as the potentiodynamic polarization and EIS tests only reflect instantaneous corrosivity under applied voltage.

Two-dimensional (2D) potential diagrams for the samples annealed at 120, 150, and 240 °C alloys are shown in Fig. 10 to verify the influence of phase precipitation on the corrosion properties of alloy wires. The diagrams reveal that the precipitated phases had different Volta potentials compared to the matrix, indicating their susceptibility to pitting corrosion. Notably, $Ag_{17}Mg_{54}$ demonstrated a larger potential difference with the α-Mg matrix (80−100 mV) compared to Mg_2Zn_{11} (30−50 mV). This demonstrates that the $Ag_{17}Mg_{54}$ phase had a more pronounced effect in accelerating the corrosion rate. The $Ag_{17}Mg_{54}$ phase was preferentially etched as the micro anode, while the α-Mg was regarded as the cathode. Based on the Volta potential analysis of the $Ag_{17}Mg_{54}$ and α-Mg matrix, a strong galvanic coupling was formed between them. SKPFM results show no obvious difference in corrosion rates among the alloy wires annealed at different temperatures.

4 Discussion

4.1 Effect of annealing temperature on mechanical properties

The experimental results indicated the significant influence of annealing temperature on the mechanical properties of Mg−3Zn−0.2Ca−2Ag alloy wire. Firstly, grain boundaries are a significant obstacle to dislocation movement, leading to boundary strengthening effects [35,36], which can be described using the Hall−Petch relationship [12]: $\sigma_{GB}=\sigma_0+kd^{-1/2}$. Increasing annealing temperature caused a significant increase in grain size, diminishing the grain boundary strengthening effect and leading to strength reduction. Moreover, the un-DRXed region, caused by large deformation, decreased with increasing annealing temperature until it disappeared. Secondly, the bimodal microstructure is also related to the mechanical properties. The fine DRXed grains enhanced the TYS through grain boundary strengthening, and the relatively random orientation was conducive to substrate slip during stretching. Therefore, small DRXed grains with relatively random orientations improved strength and ductility simultaneously [37], with alloy wires annealed at 150 °C, exhibiting higher strength and maximum ductility. The dense substructure in un-DRXed grains serves as a barrier for dislocation movement [38]. Annealing gradually eliminates internal stress and dislocations but retains some lattice distortions and GND. The effect of dislocations on yield strength can be calculated by $\sigma_{dislo}=M\alpha G b\sqrt{\rho_{GND}}$ [12]. According to the formula, as the annealing temperature increases,

Table 4 Equivalent circuit fitting data of Mg−3Zn−0.2Ca−2Ag alloy wires annealed at different temperatures in SBF solution

Temperature/ °C	R_s/ ($\Omega\cdot cm^2$)	CPE_{dl}		R_{ct}/ ($\Omega\cdot cm^2$)	CPE_f		R_f/ ($\Omega\cdot cm^2$)	L/ ($H\cdot cm^2$)	R_L/ ($\Omega\cdot cm^2$)
		Y_1/($\mu F\cdot cm^2$)	n_1		Y_2/($\mu F\cdot cm^2$)	n_2			
120	6.299	163.52×10^{-4}	0.227	300	10.074×10^{-5}	0.807	72	112	220
150	7.569	26.24×10^{-4}	0.331	448	5.521×10^{-5}	0.832	167	863	569
240	12.7	4.45×10^{-4}	0.460	185	18.265×10^{-5}	0.827	77	500	1241

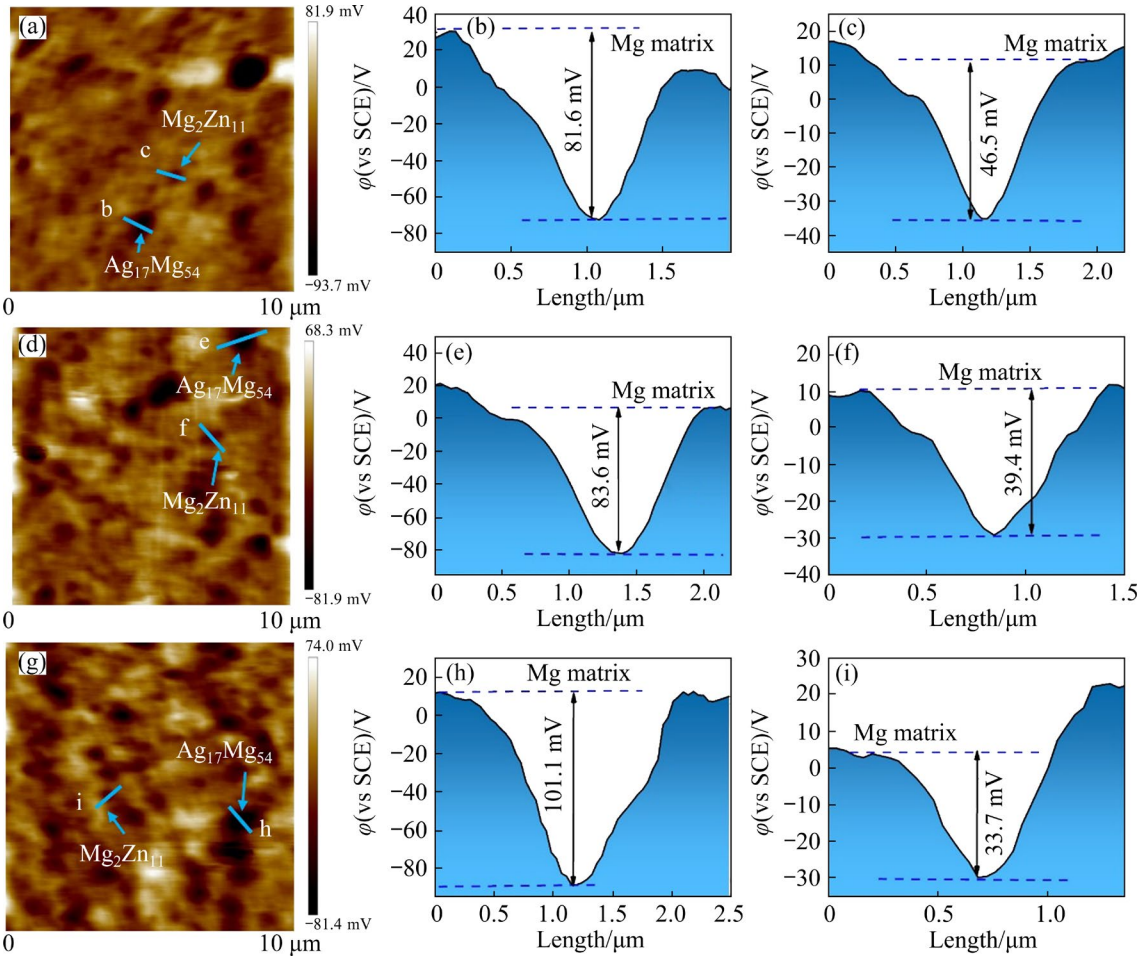

Fig. 10 SKPFM analysis of Mg−3Zn−0.2Ca−2Ag alloy wires annealed at different temperatures: (a) Surface Volta potential mappings for samples annealed at 120 °C; (b, c) Potential difference diagram of selected line segment in (a); (d) Surface Volta potential mappings for samples annealed at 150 °C; (e, f) Potential difference diagram of selected line segment in (d); (g) Surface Volta potential mappings for samples annealed at 240 °C; (h, i) Potential difference diagram of selected line segment in (g)

GND decreases, and yield strength decreases (Fig. 4). Thirdly, precipitation hardening is a promising mechanism for developing high-strength Mg alloys [39,40]. A large number of Mg_2Zn_{11} and $Ag_{17}Mg_{54}$ particles provide dispersion strengthening [41,42]. For alloy wires annealed at 150 °C, a uniform distribution of nanoscale precipitates Mg_2Zn_{11} was observed, enhancing strength without a significant plasticity reduction [43]. In addition, the second phase contributed to grain refinement. As the temperature increased in this study, the volume fraction of the second phase decreased, resulting in a decrease in the precipitation strengthening effect. In conclusion, higher annealing temperature led to increased grain size, dynamic recrystallization degree, reduced dislocation density, and volume fraction of the second phase, ultimately contributing to decreased strength.

Annealing temperature significantly affects elongation. Due to non-uniform strain during drawing, most grains exhibited irregular (or non-equiaxial) profiles and numerous curved grain boundaries under short-time annealing at a low temperature of 120°C, indicating that these grains were in an unbalanced state. Studies have shown that the microstructure composed of uneven and unbalanced grains cannot provide good uniform deformation ability, which is unfavorable to the elongation [44,45]. Therefore, the alloy wire annealed at 120 °C showed poor plasticity. In contrast, as the temperature rose to 150 and 240 °C, the uniformity and regularity of recrystallized grains improved, enhancing plasticity. The alloy wires annealed at 150 °C achieved a balance of strength and plasticity due to their uniform and fine

grain structure. Although the alloy wires annealed at 240 °C underwent recrystallization, their coarse grains were prone to intergranular deformation, leading to a decrease in plasticity. Additionally, the weaker texture and lower dislocation density of alloy wires annealed at 150 °C contributed to their superior plasticity.

4.2 Effect of annealing temperature on corrosion behavior

As primary sites of crystallographic defects, grain boundaries are prone to corrosion due to atoms existing in an unstable, semi-activated state, making them easily separable from the matrix. When the magnesium alloy wires came into contact with the SBF solution, the corrosion preferentially occurred at grain boundaries. A smaller grain size leads to a higher density of preferentially corroded grain boundaries. The corrosion resistance improved with a more uniform corrosion film. Large deformation in Mg−Zn−Ca−Ag alloy induced defects and residual stress, which could be relieved by annealing. Stress corrosion cracking increased with residual stress. The alloy wire annealed at 150 °C, with uniform fine grains and lower internal stress, theoretically exhibited a lower degradation rate and more uniform corrosion morphology. In contrast, the alloy wires annealed at 120 °C retained dislocations and stress concentrations, promoting local corrosion and reducing corrosion resistance. Despite the lowest internal stress in alloy wires annealed at 240 °C, their large grain size limited significant improvement in corrosion resistance.

As shown in Fig. 10, the potential of the precipitated phase was different from that of the Mg matrix, which was prone to causing galvanic corrosion. Stress concentration facilitated the precipitation of the second phase. Low-temperature annealing, acting as artificial aging, enhanced galvanic corrosion by forming more corrosion pairs. A high annealing temperature (240 °C) dissolved small second phase particles back into the matrix, while a short annealing time retained larger particles, intensifying local corrosion and compromising resistance. However, the nano Mg_2Zn_{11} phase from the alloy wires annealed at 150 °C was uniformly distributed, forming a uniform corrosion-resistant film. In summary, the alloy wires with uniform fine grains, less internal stress, and well-distributed nano Mg_2Zn_{11} phase exhibited improved corrosion resistance. Our study revealed a higher degradation rate of the alloy wire compared to existing magnesium alloy (Fig. 6(b)), which is attributed to large $Ag_{17}Mg_{54}$ phases. Figure 6 depicts the significant potential difference between these large-sized second phases and the matrix, leading to preferential corrosion and the formation of corrosion pits, exacerbating the corrosion process. Furthermore, the uniform distribution of fine Mg_2Zn_{11} phases contributes to a uniform corrosion-resistant film. However, the primary reason for the accelerated corrosion rate remains the preferential detachment of large-sized $Ag_{17}Mg_{54}$ phases.

5 Conclusions

(1) Mg−3Zn−0.2Ca−2Ag alloy wires, annealed at different temperatures, exhibited the same second phase, but its amount decreased gradually at higher temperatures. As the temperature rose, the non-recrystallized area diminished, grain size increased, and dislocation density significantly decreased.

(2) With increasing temperature, the grain boundary, dislocation, dispersion strengthening effects, and the contribution of un-DRXed gradually diminished. In other words, higher annealing temperatures led to a gradual decrease in wire strength. As the temperature rose, grains approached an equilibrium state. Continued temperature increase resulted in coarse grains and significantly reduced dislocation density, leading to an initial increase and subsequent decrease in plasticity.

(3) Annealing temperature significantly influenced the corrosion rate. Cl^- ions in the SBF solution punctured the $Mg(OH)_2$ protective film on magnesium alloy wires, accelerating corrosion. The finer and more evenly distributed second phase of the alloy wire annealed at 150 °C inhibited further corrosion by promoting a uniform distribution of corrosion products.

CRediT authorship contribution statement

Qing-hui WANG: Conceptualization, Methodology, Validation, Formal analysis, Investigation, Writing − Original draft preparation, Writing − Review & editing; **Shan-shan LIANG:** Writing − Review & editing, Project administration; **Fu-song YUAN:** Conceptualization, Supervision; **Bo PAN:** Writing − Review & editing,

Project administration; **Peng-fei SUN:** Investigation; **Jin-hui WANG:** Writing − Review & editing; **Bo-yu LIU:** Resources; **Hong-xiang LI:** Conceptualization, Writing − Review & editing, Funding acquisition, Supervision, Project administration.

Declaration of competing interest

The authors declare that they have no known competing financial interests or personal relationships that could have appeared to influence the work reported in this paper.

Acknowledgments

The National Natural Science Foundation of China (Nos. 51971020, 52171097), the Major State Research and Development Program of China (No. 2021YFB3701100), Key Scientific Research Project in Shanxi Province, China (No. 202102050201003), and the Opening Research Fund of State Key Laboratory for Advanced Metals and Materials, China (No. 2023-Z03), are deeply appreciated for their financial support. The authors also thank the support from the Beijing Laboratory of Metallic Materials and Processing (China) for Modern Transportation.

References

[1] WU Hong-liu, ZHAO Chang-li, NI Jia-hua, ZHANG Shao-xiang, LIU Jing-yi, YAN Jun, CHEN Yi-gang, ZHANG Xiao-nong. Research of a novel biodegradable surgical staple made of high purity magnesium [J]. Bioactive Materials, 2016, 1(2): 122−126.

[2] ZHENG Y F, GU X N, WITTE F. Biodegradable metals [J]. Materials Science and Engineering: R, 2014, 77: 1−34.

[3] QU Su, XIA Jia-zeng, YAN Jun, WU Hong-liu, WANG Hao, YI Yi, ZHANG Xiao-nong, ZHANG Shao-xiang, ZHAO Chang-Li, CHEN Yi-gang. In vivo and in vitro assessment of the biocompatibility and degradation of high-purity Mg anastomotic staples [J]. Journal of Biomaterials Applications, 2017, 31(8): 1203−1214.

[4] MAO Lin, ZHOU Hao, CHEN Li, NIU Jia-lin, ZHANG Lei, YUAN Guang-yin, SONG Cheng-li. Enhanced biocompatibility and long-term durability in vivo of Mg−Nd−Zn−Zr alloy for vascular stent application [J]. Journal of Alloys and Compounds, 2017, 720: 245−253.

[5] MAO Lin, SHEN Li, CHEN Jia-hui, ZHANG Xiao-bo, KWAK M, WU Yu, FAN Rong, ZHANG Lei, PEI Jia, YUAN Guang-yin, SONG Cheng-li, GE Jun-bo, DING Wen-jiang. A promising biodegradable magnesium alloy suitable for clinical vascular stent application [J]. Scientific Reports, 2017, 7: 46343.

[6] ZHANG Yue, CAO Jian, LU Meng-meng, SHAO Yi, JIANG Ke-wei, YANG Xiao-dong, XIONG Xiao-yu, WANG Shan, CHU Cheng-lin, XUE Feng, YE Ying-jiang, BAI Jing. A biodegradable magnesium surgical staple for colonic anastomosis: In vitro and in vivo evaluation [J]. Bioactive Materials, 2023, 22: 225−238.

[7] MA Ying-zhong. Alloying rules, microstructure and properties of Mg−Zn−Ca−X alloy with high strength, high toughness and controllable degradation rate applied as anastomotic nails [D]. Beijing: Beijing University of Science and Technology, 2022. (in Chinese)

[8] MA Ying-zhong, WANG De-xin, LI Hong-xiang, YANG Chang-lin, YUAN Fu-song, ZHANG Ji-shan. Microstructure, mechanical properties and corrosion behavior of quaternary Mg−1Zn−0.2Ca−*x*Ag alloy wires applied as degradable anastomotic nails [J]. Transactions of Nonferrous Metals Society of China, 2021, 31(1): 111−124.

[9] WANG Qing-hui, LIANG Shan-shan, YUAN Fu-song, LIU Bo-yu, YU Jun-zhi, WANG Wei, FAKHAR N, LI Hong-xiang. A high-performance degradable Mg alloy suturing staple for single-arm oral stapling robot [J]. Journal of Magnesium and Alloys, 2024, 12: 4096−4118.

[10] SHEVTSOV P N, SHEVTSOVA E F, BURBAEVA G S. Effect of aluminum, iron, and zinc ions on the assembly of microtubules from brain microtubule proteins [J]. Bulletin of Experimental Biology and Medicine, 2016, 161(4): 451−455.

[11] NAKAMURA Y, TSUMURA Y, TONOGAI Y, SHIBATA T, ITO Y. Differences in behavior among the chlorides of seven rare earth elements administered intravenously to rats [J]. Fundamental and Applied Toxicology, 1997, 37: 106−116.

[12] ZHANG Hong-fei, DING Yu-tian, LI Rui-min, SHEN Yue, LEI Jian. Achieving exceptional improvement of yield strength in Mg−Zn−Ca alloy wire by nanoparticles induced by extreme plastic deformation [J]. Materials Science and Engineering: A, 2022, 853: 143733.

[13] LU Y, BRADSHAW A R, CHIU Y L, JONES I P. Effects of secondary phase and grain size on the corrosion of biodegradable Mg−Zn−Ca alloys [J]. Materials Science and Engineering: C, 2015, 48: 480−486.

[14] CEN-EN ISO 10993-15. Biological evaluation of medical devices — Part 15. Identification and quantification of degradation products from metals and alloys [S]. 2023.

[15] ZHANG Shao-xiang, ZHANG Xiao-nong, ZHAO Chang-li, LI Jia-nan, SONG Yang, XIE Chao-ying, TAO Hai-rong, ZHANG Yan, HE Yao-hua, JIANG Yao, BIAN Yu-jun. Research on an Mg−Zn alloy as a degradable biomaterial [J]. Acta Biomaterialia, 2010, 6(2): 626−640.

[16] BAKHSHESHI-RAD H R, IDRIS M H, ABDUL-KADIR M R, OURDJINI A, MEDRAJ M, DAROONPARVAR M, HAMZAH E. Mechanical and bio-corrosion properties of quaternary Mg−Ca−Mn−Zn alloys compared with binary Mg−Ca alloys [J]. Materials & Design, 2014, 53: 283−292.

[17] RAD H R B, IDRIS M H, KADIR M R A, FARAHANY S. Microstructure analysis and corrosion behavior of biodegradable Mg−Ca implant alloys [J]. Materials & Design, 2012, 33: 88−97.

[18] ZENG Rong-chang, ZHANG Jin, HUANG Wei-jiu, DIETZEL W, KAINER K U, BLAWERT C, KE Wei. Review of studies on corrosion of magnesium alloys [J]. Transactions of Nonferrous Metals Society of China, 2006, 16: s763−s771.

[19] AMANO H, HANADA K, HINOKI A, TAINAKA T, SHIROTA C, SUMIDA W, YOKOTA K, MURASE N,

OSHIMA K, CHIBA K, TANAKA Y, UCHIDA H. Biodegradable surgical staple composed of magnesium alloy [J]. Scientific Reports, 2019, 9(1): 14671.

[20] BAI Jing, YIN Ling-ling, LU Ye, GAN Yi-wei, XUE Feng, CHU Cheng-lin, YAN Jing-li, YAN Kai, WAN Xiao-feng, TANG Zhe-jun. Preparation, microstructure and degradation performance of biomedical magnesium alloy fine wires [J]. Progress in Natural Science: Materials International, 2014, 24(5): 523−530.

[21] TIAN Yuan, MIAO Hong-wei, NIU Jia-lin, HUANG Hua, KANG Bin, ZENG Hui, DING Wen-jiang, YUAN Guang-yin. Effects of annealing on mechanical properties and degradation behavior of biodegradable JDBM magnesium alloy wires [J]. Transactions of Nonferrous Metals Society of China, 2021, 31(9): 2615−2625.

[22] LUAN Yu. Research on hot drawing process, microstructure and properties of ZN20 magnesium alloy [D]. Shenyang: Shenyang University of Technology, 2021. (in Chinese)

[23] CHEN Kai, LU Yun, TANG Hong-yan, GAO Yuan-ming, ZHAO Feng, GU Xue-nan, FAN Yu-bo. Effect of strain on degradation behaviors of WE43, Fe and Zn wires [J]. Acta Biomaterialia, 2020, 113: 627−645.

[24] SEITZ JAN-MARTEN, WULF ERIC, FREYTAG PATRIK, BORMANN DIRK, BACH FRIEDRICH-WILHELM. The manufacture of resorbable suture material from magnesium [J]. Advanced Engineering Materials, 2010, 12(11): 1099−1105.

[25] YAN Kai, SUN Jia-peng, BAI Jing, LIU Huan, HUANG Xin, JIN Zhao-yang, WU Yu-na. Preparation of a high strength and high ductility Mg−6Zn alloy wire by combination of ECAP and hot drawing [J]. Materials Science and Engineering: A, 2019, 739: 513−518.

[26] CAI Hong, ZHANG Yue, LI Xuan, MENG Jiao, XUE Feng, CHU Cheng-lin, TAO Li, BAI Jing. Self-reinforced biodegradable Mg−2Zn alloy wires/polylactic acid composite for orthopedic implants [J]. Composites Science and Technology, 2018, 162: 198−205.

[27] ZHENG Mao-bo. Study on the preparation, microstructures and properties of Mg−Zn−Ca alloy wire for biomaterial application [D]. Tianjin: Tianjin University of Technology, 2018. (in Chinese)

[28] HUANG Fu-yu. Microstructure, mechanical properties and corrosion resistance of Mg−Zn alloy wires for medical use [D]. Yangzhou: Yangzhou University, 2021. (in Chinese)

[29] XING Fei, LI Shang, YIN Dong-di, XIE Ji-chang, ROMMENS P M, XIANG Zhou, LIU Ming, RITZ U. Recent progress in Mg-based alloys as a novel bioabsorbable biomaterials for orthopedic applications [J]. Journal of Magnesium and Alloys, 2022, 10(6): 1428−1456.

[30] VINOGRADOV A, MERSON E, MYAGKIKH P, LINDEROV M, BRILEVSKY A, MERSON D. Attaining high functional performance in biodegradable Mg−alloys: An overview of challenges and prospects for the Mg−Zn−Ca system [J]. Materials, 2023, 16(3): 1324.

[31] SONG Ming-shi, ZENG Rong-chang, DING Yun-fei, LI R W, EASTON M, COLE I, BIRBILIS N, CHEN Xiao-bo. Recent advances in biodegradation controls over Mg alloys for bone fracture management: A review [J]. Journal of Materials Science & Technology, 2019, 35(4): 535−544.

[32] LI Chuan-qiang, TONG Zhi-pei, HE Yi-bin, HUANG Huai-pei, DONG Yong, ZHANG Peng. Comparison on corrosion resistance and surface film of pure Mg and Mg−14Li alloy [J]. Transactions of Nonferrous Metals Society of China, 2020, 30(9): 2413−2423.

[33] LI C Q, XU D K, ZENG Z R, WANG B J, SHENG L Y, CHEN X B, HAN E H. Effect of volume fraction of LPSO phases on corrosion and mechanical properties of Mg−Zn−Y alloys [J]. Materials & Design, 2017, 121: 430−441.

[34] LIU Jin-hui, SONG Ying-wei, CHEN Jia-chen, CHEN Peng, SHAN Da-yong, HAN En-Hou. The special role of anodic second phases in the micro-galvanic corrosion of EW75 Mg alloy [J]. Electrochimica Acta, 2016, 189: 190−195.

[35] LUO Bao-min, LI Dao-xi, ZHAO Chao, WANG Zhi, LUO Zong-qiang, ZHANG Wei-wen. A low Sn content Cu−Ni−Sn alloy with high strength and good ductility [J]. Materials Science and Engineering: A, 2019, 746: 154−161.

[36] VENKATALAXMI A, PADMAVATHI B S, AMARANATH T. A general solution of unsteady Stokes equations [J]. Fluid Dynamics Research, 2004, 35(3): 229−236.

[37] OH-ISHI K, MENDIS C L, HOMMA T, KAMADO S, OHKUBO T, HONO K. Bimodally grained microstructure development during hot extrusion of Mg−2.4Zn−0.1Ag−0.1Ca−0.16Zr (at.%) alloys [J]. Acta Materialia, 2009, 57: 5593−5604.

[38] SEDLÁČEK R, BLUM W, KRATOCHVÍL J, FOREST S. Subgrain formation during deformation: Physical origin and consequences [J]. Metallurgical and Materials Transactions A: Physical Metallurgy and Materials Science, 2002, 33: 319−327.

[39] NIE Jian-feng. Precipitation and hardening in magnesium alloys [J]. Metallurgical and Materials Transactions A: Physical Metallurgy and Materials Science, 2012, 43: 3891−3939.

[40] WANG Fu-lin, BHATTACHARYYA J J, AGNEW S R. Effect of precipitate shape and orientation on Orowan strengthening of non-basal slip modes in hexagonal crystals, application to magnesium alloys [J]. Materials Science and Engineering: A, 2016, 666: 114−122.

[41] LI Rong-guang, LI Hao-ran, PAN Hu-cheng, XIE Dong-sheng, ZHANG Jing-huai, FANG Da-qing, DAI Yong-qiang, ZHAO Dong-yue, ZHANG Hang. Achieving exceptionally high strength in binary Mg−13Gd alloy by strong texture and substantial precipitates [J]. Scripta Materialia, 2021, 193: 142−146.

[42] PAN Hu-cheng, KANG Rui, LI Jing-ren, XIE Hong-bo, ZENG Zhuo-ran, HUANG Qiu-yan, YANG Chang-lin, REN Yu-ping, QIN Gao-wu. Mechanistic investigation of a low-alloy Mg−Ca-based extrusion alloy with high strength−ductility synergy [J]. Acta Materialia, 2020, 186: 278−290.

[43] HAN Gang, XIE Zhen-jia, LEI Bao, LIU Wen-qing, ZHU H H, YAN Yu, MISRA R D K, SHANG Cheng-jia. Simultaneous enhancement of strength and plasticity by nano *B*2 clusters and nano-γ phase in a low carbon low alloy steel [J]. Materials Science and Engineering: A, 2018, 730: 119−136.

[44] SUN Liu-xia, BAI Jing, YIN Ling-ling, GAN Yi-wei, XUE Feng, CHU Cheng-lin, YAN Jing-li, WAN Xiao-feng, DING

Hong-yan, ZHOU Guang-hong. Effect of annealing on the microstructures and properties of cold drawn Mg alloy wires [J]. Materials Science and Engineering: A, 2015, 645: 181−187.

[45] ZHANG Xiao-bo, YUAN Guang-yin, MAO Lin, NIU Jia-lin, FU Peng-huai, DING Wen-jiang. Effects of extrusion and heat treatment on the mechanical properties and biocorrosion behaviors of a Mg−Nd−Zn−Zr alloy [J]. Journal of the Mechanical Behavior of Biomedical Materials, 2012, 7: 77−86.

退火温度对可降解 Mg−3Zn−0.2Ca−2Ag 合金丝力学性能和腐蚀行为的影响

王庆慧[1]，梁姗姗[2]，原福松[2]，潘 博[3]，孙鹏飞[3]，王金辉[1]，刘伯禹[1]，李宏祥[1]

1. 北京科技大学 新金属材料国家重点实验室，北京 100083；
2. 北京大学 口腔医院 口腔医学数字化研究中心，北京 100081；
3. 中国医学科学院&北京协和医学院 整形外科医院，北京 100144

摘 要：口腔和颌面外科手术对可降解镁钉的需求不断增加，为满足这一需求，报道了高性能 Mg−3Zn−0.2Ca−2Ag 合金丝，探讨退火温度对合金丝力学性能和腐蚀行为的影响。结果显示，随着退火温度的升高，晶粒增大，第二相体积分数减少，位错密度降低，导致强度下降。经 150 ℃ 退火的合金丝的晶粒均匀细小且位错密度较低，具有最高的伸长率(19.6%)。微观观察及电化学和浸泡测试显示退火温度显著影响腐蚀速率。经 150 ℃退火的合金丝具有优异的耐蚀性，这主要是因为晶粒细小而均匀、应力低以及均匀分布的纳米第二相。最终，经 150 ℃退火的合金丝表现出更好的综合性能，有望成为可降解镁钉的理想材料。

关键词：生物可降解镁合金；镁吻合钉；力学性能；电偶腐蚀；生物相容性

(Edited by Xiang-qun LI)